AIAA JOURNAL
Vol. 49, No. 5, May 2011

Evaluation of a Vortex Generator Model in Adverse Pressure Gradient Boundary Layers

Florian von Stillfried,* Stefan Wallin,† and Arne V. Johansson‡
Royal Institute of Technology, 100 44 Stockholm, Sweden

DOI: 10.2514/1.J050680

The use of a two-dimensional statistical passive vortex generator model, applied to an adverse pressure gradient boundary-layer flow, is evaluated qualitatively against experimental and fully resolved vortex generator computations. The modeling approach taken here has the advantage of substantially reducing the complexity of including such flow separation control devices in a computational mesh, thus giving the opportunity to carry out faster parametric studies. Additional stresses, originating from the vortex generator model approach, are added as additional turbulent stresses to the mean governing equations instead of resolving vortex structures in the computational domain. The vortex generator model has been applied to allow direct comparison with prior experiments carried out at the Royal Institute of Technology Stockholm. Variations of the vortex generator streamwise position and tests of different vortex generator setups, such as co- and counter-rotational settings, are presented. Distributions of wall-pressure and skin-friction coefficients are used to evaluate the vortex generator model against fully resolved vortex generator data. It is shown that the vortex generator model successfully predicts attached and separated flow states. Moreover, the results illustrate the vortex generator model's capability to predict flow control sensitivity with respect to the streamwise position.

Nomenclature

c = vortex generator/wing chord length
c_f = local skin friction coefficient
c_p = local wall pressure coefficient
D = mean distance between neighboring vortex generator pairs
d = mean distance between vanes of a single vortex generator pair
H_{12} = shape factor δ^*/θ
h = height
K = local airfoil section lift slope
l = length
Re = Reynolds number
r_0 = vortex core radius
U_i = mean streamwise velocity field
$\overline{u'_i u'_j}$ = time/spanwise averaged Reynolds stresses
$u_\Phi(r)$ = azimuthal vortex-induced velocity field
$V_i(y, z)$ = total induced vortex velocity field
$V_\Phi(r)$ = azimuthal single vortex velocity field
x = streamwise coordinate
y = wall-normal coordinate
z = spanwise coordinate
α = angle of attack/incidence
α_1 = modified α_1 parameter in differential Reynolds stress transport model
Γ = circulation
γ_e = circulation per unit width
$\Delta\overline{u'_i u'_j}$ = time/spanwise averaged vortex stresses
δ^* = displacement thickness
δ_{99} = 99% boundary-layer thickness
θ = momentum thickness
χ = backflow coefficient

Subscripts

att = attachment point value
end = ending coordinate
exp = experiment value
max = maximum value
sep = separation point value
start = starting coordinate
VG = vortex generator value
wall = wall value
∞ = freestream value

I. Introduction

THE use of flow control in modern engineering applications is common since flow control devices have successfully shown to prevent and delay flow separation in wall-bounded flows, such as those occurring in inlet ducts, in diffusers, or on aircraft wings. The application of passive vortex generator (VG) vanes typically energizes low-momentum boundary-layer flow by means of increased momentum mixing near walls. Because of delayed or even vanished separation, positive effects are very often lower overall drag generation through attached flow, decreased loads, lower design weight, and increased efficiency. Negative aspects also occur, mostly in the form of parasitic drag when flow separation control is not needed and if the passive VGs cannot be retracted. However, such a tradeoff situation often favors the use of passive VGs due to their overall advantages.

One of the first comprehensive papers about flow separation control for airfoils and wings was published by Pearcey [1]. It includes a chapter about VGs, their mechanism, types and design criteria for flow control. Pearcey discusses different kinds of VG systems such as corotating, counter-rotational settings, different types of VG geometries, and a discussion about the influence of vortex strength and VG scale. The importance of vortex paths for counter-rotational systems due to induced vortex velocities as well as the importance of spacing issues for corotating systems due to velocity damping effects are described. Pearcey used the generated drag of the VGs as a defining parameter for successful and

---

Received 21 May 2010; revision received 19 November 2010; accepted for publication 30 November 2010. Copyright © 2010 by Florian von Stillfried. Published by the American Institute of Aeronautics and Astronautics, Inc., with permission. Copies of this paper may be made for personal or internal use, on condition that the copier pay the $10.00 per-copy fee to the Copyright Clearance Center, Inc., 222 Rosewood Drive, Danvers, MA 01923; include the code 0001-1452/11 and $10.00 in correspondence with the CCC.

*Graduate Student, Linné Flow Center, Department of Mechanics, KTH Mechanics; florian@mech.kth.se. Member AIAA.

†Senior Scientist, Linné Flow Center, Department of Mechanics, FOI Defense and Security, Systems and Technology, KTH Mechanics; stefan.wallin@foi.se.

‡Professor, Linné Flow Center, Department of Mechanics, KTH Mechanics; johansson@mech.kth.se. Member AIAA.

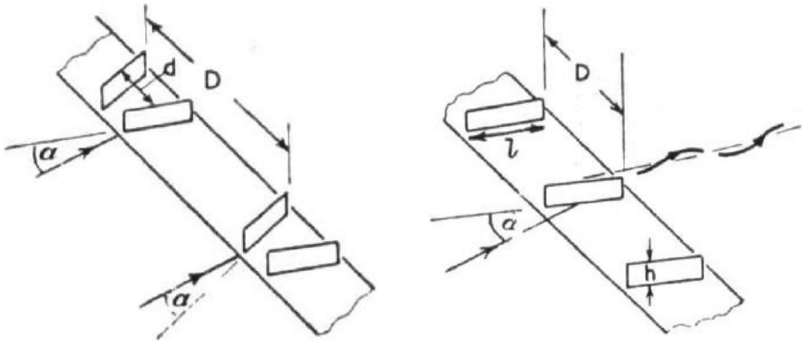

Fig. 1 Pearcey's notation of VGs [1].

unsuccessful VG designs. Pearcey's successful designs for the application on aircraft wings and airfoils have a VG height-to-wing-chord ratio $h/c = 0.01$, $D/d = 4$, $D/h = 10$, $l/h = 1.25$ and 2.5 at an angle of incidence $\alpha = \pm 15°$ which are close to the VG parameters used in the present study (see also Fig. 1, with Pearcey's notation). Note that the authors use a slightly different notation throughout the paper.

Pauley and Eaton [2] experimentally investigated vortex structures originating from delta-shaped VGs in counter-rotational common-flow-up/down and corotating setups with a height of approximately 150% of the local boundary-layer thickness δ_{99}. VGs were mounted within a zero pressure gradient (ZPG) turbulent boundary layer on a flat plate at a momentum thickness Reynolds number $Re_\theta = 1700$. Pauley and Eaton studied the downstream development of the interacting vortex structures by an investigation of the streamwise vorticity and circulation. They found out that a common-flow-up setting leads to higher vortex interaction compared with a common-flow-down setting. They concluded that vorticity is diffused more quickly when there are strong interactions with neighboring vortices. This leads to a larger decrease in vorticity for common-flow-up VG pairs. Moreover, the primary mechanism for decreasing circulation was found to be the spanwise component of the skin friction. Since common-flow-down VGs interact more strongly with the viscous near-wall flow, it was concluded that this setting is likely to lose more circulation strength than common-flow-up VGs.

Godard and Stanislas [3] carried out an experimental study regarding optimal parameters for VGs in a decelerating boundary layer. Skin friction plots were used in order to characterize the VG effectiveness on flow separation control. They investigated several VG parameters such as the height, the shape, the position, the spanwise spacing, and the blade distance of counter-rotational paired devices. Corotating devices were also included in this study, yet not as comprehensively as counter-rotational VGs, because counter-rotational devices turned out to perform better than corotating devices, leading to twice the skin friction increase. In particular, the VG shape has importance for the flow control effectiveness to prevent separation since triangular VGs had advantages over rectangular VGs. The skin friction c_f is also sensitive to the VG vane angle of incidence α_{VG}, leading to an optimal value of $\alpha_{\mathrm{VG}} \approx 18°$. On the other hand, other parameters like the VG aspect ratio and the VG streamwise position did not show large influence on the results. In total, Godard and Stanislas showed that skin friction measurements are an appropriate and sufficiently sensitive way for the investigation of passive VGs for flow separation control. Furthermore, they present optimal parameters for co- and counter-rotational VG arrays.

In accordance with Lin [4], the VG parameters by Godard and Stanislas [3] are very close to optimal values. Lin on the other hand has presented a comprehensive overview of ongoing research within the area of subboundary-layer VGs (SBVG), stating that it is necessary to reduce the height h_{VG} of such devices to a maximum of 50% of the local boundary-layer thickness δ_{99} in order to maximize efficiency and decrease parasitic drag production. Lin [4] also presents research of numerous different shapes and system settings regarding their effectiveness in terms of the percent reduction of the separation region and streamwise pressure distributions. Furthermore, different aerodynamic applications for flow control such as a high-lift airfoils, swept wings, noise reduction, and engine inlets are summarized and presented in the paper in which different methods to determine efficiency (lift/pressure/drag coefficient plots, sound pressure levels, etc., depending on the application) were used. Lin comes to the conclusion that SBVGs with device heights of $0.1 \leq h_{\mathrm{VG}}/\delta_{99} \leq 0.5$ are most effective and efficient when separation regions are fixed. To increase efficiency for VGs, the approach of minimal near-wall protuberances, i.e., the avoidance of unnecessary large VGs is highly desired. By that, vortex generation with just the necessary vortex strength in order to overcome separation effects is enabled. Furthermore, corotating VGs should have sufficient space between the vanes, enabling the reduction of vortex interaction and decay.

Computational fluid dynamics (CFD) introduces additional challenges to the investigation of passive VG vanes. Here, it is common to introduce VGs by resolved structures in the generated mesh. This is a very direct and intuitive approach, yet leading to many additional grid points in the vicinity of the VG. In turn, this implementation needs to be done carefully in order to resolve the vortex structures in the flow, leading to high design costs for the mesh generation. Moreover, parameter variations cannot be carried out easily because the mesh has to be changed according to new settings, giving rise to even higher grid generation costs the more comprehensive a parameter variation gets.

The development of VG modeling is the consequent approach that has become more and more used within the last decade. Bender et al. [5] have introduced a VG model that uses a side force source term normal to the local flow and parallel to the inlet surface. The BAY (Bender Anderson Yagle) VG model is based on the lifting line theory (LLT) [6,7] that adjusts the local flow velocity with the VG, depending on an empirical model constant which can be difficult to define correctly. Grid points that are supposed to be located within the VG vane need to be identified by the user in order to apply the forcing at the correct location. This method can be tricky since VGs commonly have an insignificant thickness. As Jirásek [8] points out, this VG model approach is therefore grid dependent. Moreover, VG arrays modeled by the BAY model are simplified to a single distributed forcing along the spanwise direction enclosing the entire VG array that forces the flow.

Jirásek [8] suggested an improved BAY model by removing some of its drawbacks, calling it the jBAY model. The two approaches have in common that their meshes require three dimensions in order to account for the forcing source term at the modeled VG position. Yet, the jBAY model removes the geometrical structures of the VGs and the forcing is applied on a zero thickness surface. Still, the application of the jBAY model is not completely grid independent. A sufficient grid resolution is needed for the region downstream of the forcing region where the generated vortex structures need to be resolved in three dimensions.

Another step towards a simplification of the application of VGs within CFD is the introduction of statistical methods as done by Törnblom and Johansson [9]. Here, a Reynolds stress approach is used in a statistical sense. Additional stresses that originate from such modeled VGs and their additional vortex velocity field are added to the differential Reynolds stress transport model (DRSM) equations. The core of this model is a Lamb–Oseen vortex model in combination with the LLT that also takes some of the VG's geometrical aspects into account. By spanwise averaging the second-order correlations of the additional vortex velocity field in the forcing plane, vortex stress contributions are formed and added to the Reynolds stress tensor. This method can be applied in two-dimensional as well as for three-dimensional meshes.

Investigations of this statistical VG model in a ZPG boundary-layer flow over a flat plate were presented in von Stillfried et al. [10] based on experiments by Lögdberg et al. [11]. A calibration of the VG model was carried out and Reynolds stress results were compared with spanwise averaged experimental data. The VG model was successfully applied on the ZPG flat plate boundary-layer flow, and in internal adverse pressure gradient (APG) diffuser flow. The investigations showed that the VG model was capable of predicting correct trends and tendencies of the mean streamwise velocity and the total pressure recovery by predicting a reasonable decreased and even vanished separation region. The VG model has also the advantage of being no more computationally expensive than solving for the original Reynolds-averaged Navier–Stokes (RANS) equations without the VG model forcing.

The main objective of this work is to examine the capabilities of the statistical VG model in APG flows over a flat plate, including a pressure-induced separation region. This flow case was previously carried out experimentally by Lögdberg et al. [12,13]. Firstly, the clean flat plate with APG is investigated and boundary conditions are adjusted in order to match experimental results, i.e., the wall pressure distribution in the streamwise direction without flow control. Then, the modeled VGs are introduced at the same position as in the experiment. Fully resolved VGs are also computed in order to gain additional comparison data for the evaluation of the VG modeling approach. Secondly, parameter variation studies of the VG streamwise position, the VG height, the VG spacing, as well as counter- and corotating VG setups are conducted using the VG model and are compared with the experimental results.

II. Implementation Methods

The VG model implementation method was presented in depth in Törnblom and Johansson [9], and in von Stillfried et al. [10]. Nevertheless, the basic ideas are briefly presented here.

The VG model approach has its origin in the Prandtl LLT [6] where the circulation distribution across a wing in free flight is given by

$$\Gamma(y) = \frac{K}{2} U(y) c(y) \left[\alpha(y) - \frac{w(y)}{U(y)} \right] \tag{1}$$

where K is the local section lift slope of the wing ($K_{\max} = 2\pi$ rad^{-1} according to thin airfoil theory), $U(y)$ is the local incoming freestream velocity, $c(y)$ the local chord length of the wing, $\alpha(y)$ the local angle of attack, and $w(y)$ the local downwash velocity. The ratio $w(y)/U(y)$ is the local induced angle of attack for small α, and the local downwash $w(y)$ reads

$$w(y) = \frac{1}{4\pi} \int_{-h}^{h} \frac{\mathrm{d}\Gamma}{\mathrm{d}y'} \frac{1}{y' - y} \, \mathrm{d}y' \tag{2}$$

Because limitations regarding the application of the LLT to VGs in wall-bounded viscous flows, the LLT is only used as an approximation for deriving the circulation distribution. Here, only $\Gamma_{\max}$, the maximum value for the circulation distribution, is used for computing the additional vortex velocity field when using a Lamb–Oseen vortex model. The azimuthal vortex velocity distribution for a single VG vane reads

$$V_{\Phi}(r) = \frac{\Gamma_{\max}}{2\pi r} \left[1 - e^{-(\frac{r}{r_0})^2}\right] \tag{3}$$

with $\Gamma_{\max}$ from the LLT circulation distribution, r_0 the vortex core radius and r the radial coordinate from the vortex center. A limitation of this vortex model is that the velocity component in the streamwise direction remains unaffected. Different approaches appear in the literature, such as Velte et al. [14] who describe helical vortex structures of longitudinal vortices for high angles of incidence $\alpha = 20$ to 40° by a simplified Batchelor [15] vortex model, taking also the streamwise velocity variation into account.

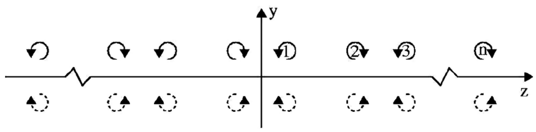

Fig. 2 A vortex array with *n* counter-rotational vortex pairs and their mirror images for computing the total superposition of the vortex-induced velocity field $V_i(y,z)$ in the VG forcing plane, figure taken from Törnblom and Johansson [9].

A VG array consists of more than one VG pair (counter-rotational setup) or more than one VG vane (corotating setup) so that all VGs influence the vortex flow field everywhere in the VG model forcing plane. Since this paper mainly discusses the investigation of counter-rotational setups, VG pairs were implemented unless stated differently. A superposition of the azimuthal vortex velocities $V_{\Phi}(r)$ for each VG pair and its corresponding vanes is needed, as shown in Fig. 2. Here, the wall ($y = 0$) acts approximately as a symmetry condition for the vortices, which is simulated by introducing mirror vortices ($y < 0$).

The additional total superimposed vortex velocity field $V_i(y,z)$ is used in order to calculate the corresponding single-point second-order statistics which are assumed to act as additional Reynolds stresses. Spanwise averaging of the second-order statistics over one VG pair distance D is used in order to derive the VG model stresses. This is sufficient because the resulting vortex flow field is periodic:

$$\Delta\overline{u_i' u_j'}(y) = \frac{1}{D} \int_{-D/2}^{D/2} V_i(y,z) V_j(y,z) \, \mathrm{d}z \tag{4}$$

Additional contributions from Eq. (4) for a VG array are only nonzero for $\Delta\overline{v'v'}$ and $\Delta\overline{w'w'}$. Moreover, a wall damping function, e.g., $(1 - \exp[-20y/h])$, needs to be introduced [9] and applied in Eq. (4) because the vortex velocities in the spanwise direction at the wall boundary $y = 0$ will not cancel out and would result in a finite value in Eq. (4). The wall damping function influences the $\Delta\overline{w'w'}(y)$ stresses in order to impose correct boundary conditions for the $\Delta\overline{w'w'}(y)$ distribution so that $\Delta\overline{w'w'}(0) = 0$. The specific choice of the wall funtion is not critical for the downstream distribution evolution since it is only assumed to act very close to the wall boundary (for $y \leq h/20$). Nevertheless, damping the local peak in the $\Delta\overline{w'w'}(y)$ distribution is preferably implemented here.

The general procedure to add the resulting vortex stresses from Eq. (4) to the DRSM equations is done via a so-called triple decomposition of the instantaneous velocity field u_i at the VG streamwise position x_{VG}. First, the additional vortex velocities $V_i(y,z)$ are added to the decomposed velocity field from the general ansatz for the RANS equations:

$$u_i(y,z,t) = U_i(y) + u_i'(y,z,t) + V_i(y,z) \tag{5}$$

where U_i and u_i' are the mean velocity and the turbulent fluctuations, respectively. One possibility is to add V_i to the mean flow U_i in a RANS computation, thus resolving the generated vortices and expressing the turbulent part u_i' through a conventional turbulence model. We will here follow a different approach where V_i is added to the turbulent fluctuations u_i'. The combined velocity field v_i' from the turbulence and vortices is defined as

$$v_i'(y,z,t) \equiv u_i'(y,z,t) + V_i(y,z) \tag{6}$$

Then, the additional time- and spanwise averaged second-order statistics of the vortex velocity field enter the RST equations by substituting the Reynolds stress tensor $\overline{u_i' u_j'}$ with the extended Reynolds stress tensor $\overline{v_i' v_j'}$, where

$$\overline{v_i' v_j'}(y) = \overline{(u_i' + V_i)(u_j' + V_j)} \qquad \approx \overline{u_i' u_j'}(y) + \Delta\overline{u_i' u_j'}(y) \tag{7}$$

where

$$\Delta\overline{u_i' u_j'}(y) \equiv \overline{V_i V_j}(y) \tag{8}$$

is written for the additional contribution from the vortex stresses. At the forcing plane where the vortices are generated, the incoming turbulence has not yet been adjusted to the vortices so that the turbulence plus the vortices can be assumed to be rather uncorrelated. Thus, cross-product terms containing the correlations $\overline{u_i' V_j}$ and $\overline{u_j' V_i}$ are assumed to be negligible.

The additional stresses $\Delta\overline{u_i' u_j'}$ at the VG model plane are added as a surface source (or line source in two-dimensional) to the RST equation. This is slightly different from the approach taken by Törnblom and Johansson [9] who used a volume force in a region close to the VG. The downstream development of the combined stresses, $\overline{v_i' v_j'}$, is then described by a RST model, which takes the development of all stress components into account. The VG model approach is suitable for the use within a RST model that naturally accounts for each Reynolds stress component. Moreover, the energy transfer between the different components is established by a RST model, enabling $\overline{u'v'}$ Reynolds stress production which is initially not forced by the VG model. This nonequilibrium relaxation process cannot be captured by eddy-viscosity models. However, a corresponding addition of the vortex kinetic energy $\Delta k = \Delta\overline{u_i' u_i'}/2$ can be added to the turbulence kinetic energy k in two-equation models such as k-ω or k-ϵ models. Such an approach can be used for explicit algebraic Reynolds stress turbulence models (EARSM) that are derived from RST models but the dynamics of the energy transfer is lost and the results should be used with caution. The user must be aware of the possible drawbacks that come with a simplification to two-equation turbulence models.

III. Experimental Setup

As previously mentioned, VGs in a counter-rotational setup in an APG boundary layer were experimentally examined by Lögdberg et al. [13] (see also Figs. 3 and 4). Each VG pair consists of two rectangular vanes of height $h_{\mathrm{VG}} = 18$ mm and a chord length $c/\cos\alpha_{\mathrm{VG}}$ with $c = 54$ mm being the projected VG chord in the streamwise direction. The vanes are mounted in pairs at angles of incidence $\alpha_{\mathrm{VG}} = \pm 15°$. The mean distance between such two blades is $d = 37.5$ mm and the distance between two adjacent VG pairs is $D = 150$ mm. The VGs are mounted in an array consisting of $n = 5$ VG pairs with their trailing edges located at $x_{\mathrm{VG}} = 1.54$ m from the leading edge of the flat plate in the test section of the boundary-layer wind tunnel at Royal Institute of Technology (KTH) Stockholm. Experimental results (case 2) show that the local boundary-layer thickness at $x_{\mathrm{VG}} = 1.54$ m is $\delta_{99} = 27.3$ mm so that the ratio $h_{\mathrm{VG}}/\delta_{99} = 0.66$. The freestream velocity U_∞ is 26.5 ± 0.1 m/s and the temperature is monitored by a temperature control system at $T = 20 \pm 0.07$°C over the cross-sectional area. The wind tunnel test section is 4.0 m long with a cross-sectional area of 0.75×0.50 m^2, and the turbulence intensity in the test section is <0.04% (see also Lindgren and Johansson [16]). A flat plate made of acrylic glass splits the wind tunnel's test section and is mounted with a distance of 0.30 m to the test section's upper wall (see Fig. 4). At the wind tunnel inlet, the test section has a height of 0.50 m which is diverged by a back side curved wall at $x = 1.25$ m downstream of the leading edge of the flat plate in order to induce the APG. Furthermore, a suction system is installed at the curved wall so that flow separation is prevented there. Another feature of the suction system is the additional capability to change the APG strength through adjusting the suction rate at the curved wall. In total, three different APG cases were performed with different suction rates. Lögdberg's case 2 with a suction rate of 12.5–13% of the incoming mass flow is used for the investigation of the VG model, since it represents the most detailed investigated experiment (see also Fig. 5). All experimental measurements were performed with particle image velocimetry. Refer to Lindgren and Johansson [16] for further details of the wind tunnel, and to Lögdberg et al. [12,13] as well as to Angele [17] for further details of the experiments, the setup and the measurement techniques.

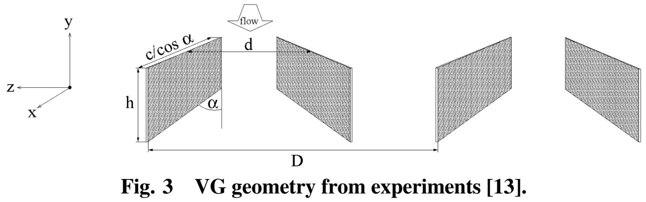

Fig. 3 VG geometry from experiments [13].

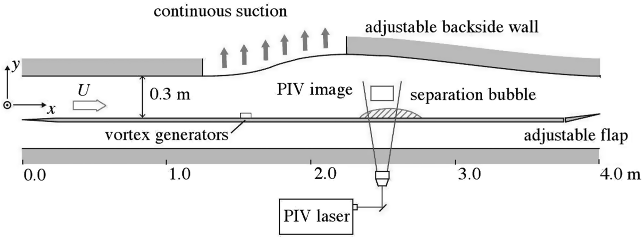

Fig. 4 Sketch of the boundary-layer wind tunnel test section used in experiments, taken from Lögdberg et al. [13].

The wall pressure coefficient c_p for all c_p diagrams is here defined as

$$c_p \equiv \frac{p - p_{\mathrm{ref}}}{q_\infty} \tag{9}$$

where p is the local wall static pressure, p_{ref} the reference wall static pressure at $x = 1.15$ m, and q_∞ the dynamic pressure in the freestream. The separation bubble in experiments is defined as the region where at least 50% back flow at the wall is developed, i.e., the wall back flow coefficient $\chi_{\mathrm{wall}} \geq 0.5$. According to Dengel and Fernholz [18], χ was extrapolated to the wall from the data points in the region $y \approx 1.5$ to 10 mm in order to estimate χ_{wall}. The resulting geometrical properties such as the separation location x_{sep}, the reattachment location x_{att}, the length l_{sep} as well as the height of the separation bubble h_{sep} [defined as $U(h_{\mathrm{sep}}) = 0$] are given in Table 1.

IV. Computational Setup

This investigation includes three computational cases: a two-dimensional case of a clean flat plate, a two-dimensional case with the VG model applied and a three-dimensional case that fully resolved the VGs on the flat plate. The following abbreviations are used for a labeling of the different computations: 1) clean flat plate

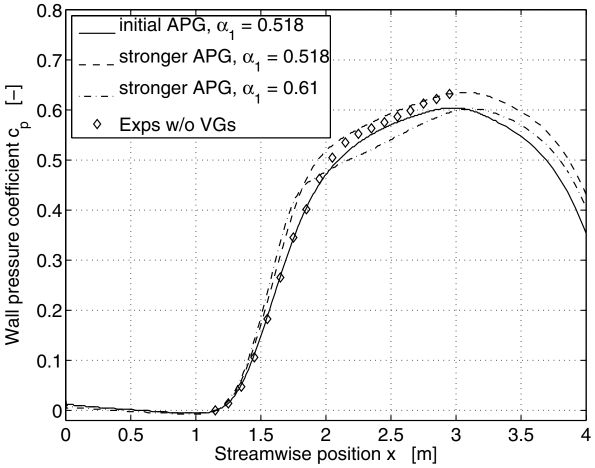

Fig. 5 Wall pressure coefficient distributions for the initial APG, the stronger APG, the stronger APG with the modified α_1 value, and the experiments without VGs (case 2 [13]).

Table 1 Separation location, reattachment location, separation bubble length, location of maximum separation bubble thickness, maximum separation bubble thickness, and the shape factor at $x_{\mathrm{sep,max}}$ of the flat plate case 2 experiments [12], and corresponding computational results of the FP2D computations with adjusted $\alpha_1 = 0.61$ given next

Case	x_{sep}, m	x_{att}, m	l_{sep}, mm	$x_{\mathrm{sep,max}}$, m	$h_{\mathrm{sep,max}}$, mm	$H_{12,\mathrm{sep,max}}$
Experiments case 2	2.24	2.85	61	2.55	17	4.90
DRSM$_{\alpha_1=0.518}$	—	—	—	—	—	—
DRSM$_{\alpha_1=0.61}$	1.91	2.42	51	2.25	26	5.63

computation (FP2D), for the flat plate without VG model; 2) VG model computation (VG2D), for the flat plate with VG model; and 3) fully resolved VG computation (VG3D), for the three-dimensional flat plate with fully resolved VGs.

Furthermore valid throughout this paper, the FP2D and VG2D computations are carried out using a differential Reynolds stress turbulence model (DRSM) with a pressure-strain rate model corresponding to the Wallin and Johansson (WJ) [19,20] EARSM with curvature correction. The WJ-DRSM is linked to the ω equation of the Hellsten k-ω turbulence model [21]. The VG3D computations are carried out by the use of the WJ-EARSM turbulence model without curvature correction [19], again linked to the Hellsten k-ω turbulence model. This is done since the VG model was specially formulated for DRSM turbulence models and because the VG3D case instead resolves the vortex structures, unlike the VG model which adds the vortex stresses to the Reynolds stresses. All computations are carried out with the Edge CFD code [22] and the local airfoil section lift slope K from Eq. (1) is set to 1.8π rad^{-1} for all VG2D computations, which is 10% lower than for the thin airfoil theory. This adjustment is justified due to the constant finite thickness of the VGs, the effects of viscosity that are present in real wall-bounded flows, and the rather large VG angle of incidence $\alpha_{\mathrm{VG}} = \pm 15°$. In addition, the modeling approach of the VGs is based on various other assumptions as described in Sec. II and the precise value of K is not critical.

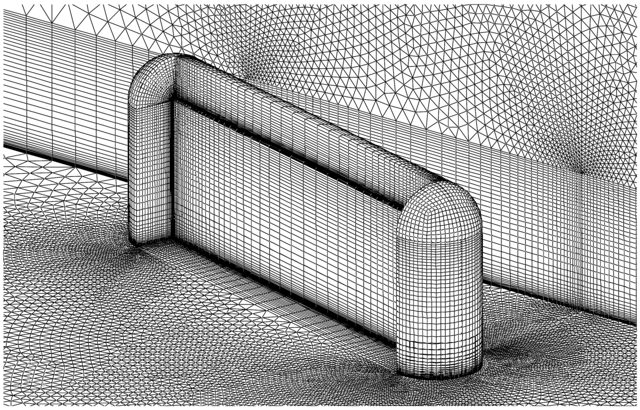

Fig. 6 O-grid and the fully resolved and meshed VG vane inside of it.

A. Boundary Conditions for Adverse Pressure Gradient Flow

For all computational cases, a 0.25-m-high and a 7.25-m-long rectangular computational domain was used. This domain includes a 0.25-m-long inflow region in front of the flat plate, thus giving a flat plate length of $l = 7.00$ m. The domain height is consequently somewhat smaller than the wind tunnel height. Instead, a specific computational boundary condition is applied on the top boundary. This strategy was applied since the upper wind tunnel wall including the suction section (see Fig. 4) could not be transformed identically into a computational domain. Therefore, pressure and velocity boundary conditions are applied at the upper boundary at $y = 0.25$ m. The upper boundary is moreover divided into two parts: first, a slip wall boundary part without pressure/velocity forcing that forces the flow in the x direction as in the wind tunnel in the experiments from the inflow region at $x = -0.25$ m up to $x = 1.25$ m in front of the APG region. Another upper boundary part from $x = 1.25$ m up to the outflow boundary at 7.00 m with weak characteristic boundary conditions where an APG/favorable pressure gradient (FPG) distribution is set in order to generate a similar wall pressure distribution on the flat plate as measured in experiments (Fig. 5). This upper boundary condition allowed mass flow across its boundary, enabling a similar APG/FPG distribution on the flat plate as in the experiments. The pressure p and the (u, v) velocities were set as boundary conditions according to inviscid theory.

For both the two- and three-dimensional grid, the value for the first grid point at the wall was set to $y = 10^{-5}$ m throughout the domain, giving values of $y^+ = \mathcal{O}(1)$. As mentioned previously, the three-dimensional computational domain fully resolved the VGs, assuming a no-slip condition not only on the flat plate but also on the VGs. In addition and in contrast to experiments, the VGs were represented by very thin structures. Furthermore, symmetry conditions were applied on both xy-boundary planes so that the computational domain could be reduced to including only one VG vane, therefore leading to a three-dimensional grid width of one half VG pair distance $D/2 = 75$ mm (see Fig. 3). Generally, the computational mesh was kept fine in the vicinity of the VGs by means of an O-grid topology and consisted in total of more than 1.9 million

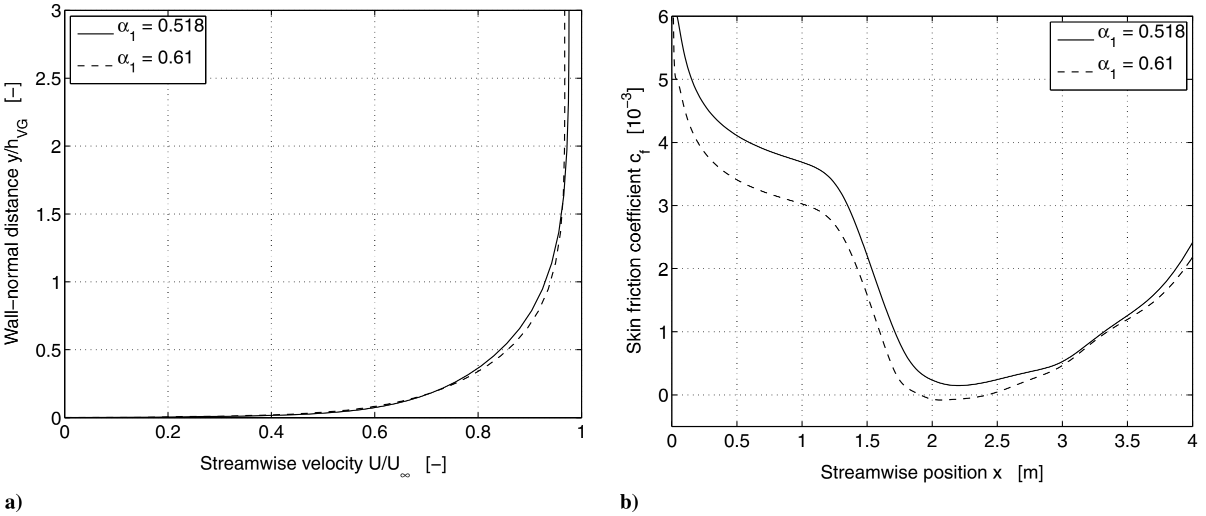

a) b)

Fig. 7 Results of the α_1 adjustment in the ω equation for the clean flat plate: a) boundary-layer velocity profiles at a streamwise position $x = 1.00$ m and b) local skin friction coefficient distributions.

nodes. A structured grid is wrapped around the VG surface. The VG surface and the O-grid outer surface can be seen in Fig. 6 and it can be observed that the structured O-grid is locally embedded in an unstructured prismatic region. Moreover, this unstructured prismatic grid is embedded in a fully structured grid upstream and downstream of the VG region (not visible in Fig. 6).

In accordance with the experiments, the freestream velocity and the temperature at the inlet are set to $U_\infty = 26.5\ \mathrm{m/s}$ and $T = 20^\circ\mathrm{C}$, respectively, giving a Reynolds number based on the plate length $Re_l \approx 1.42 \cdot 10^7$. The experimental pressure distribution on the flat plate is given between $x = 1.15$ to 2.95 m (see also Fig. 5), and therefore does not cover the whole x-coordinate range which is needed for the computations. It was decided to mirror the given wall pressure distribution around its peak value at $x_{p_{\mathrm{wall}},\max} = 2.95$ m, and a constant pressure was imposed for the region between $x = 4.75$ m and the domain outlet.

An adjustment of the α_1 coefficient for the production term in the ω equation of the Hellsten k-ω turbulence model [21] was necessary since early FP2D test runs did not generate the desired separation bubble on the flat plate, even though the wall pressure distribution was reasonably matched in the region $1.15\ \mathrm{m} < x < 1.95\ \mathrm{m}$ (initial APG, $\alpha_1 = 0.518$ in. graph in Fig. 5). Therefore, the pressure distribution on the upper boundary was forced with a slightly stronger APG in order to generate a separation region (see stronger APG $\alpha_1 = 0.518$ in. graph in Fig. 5).

Still, a separation region could not be established. A stronger amplification of the APG did not lead to any better results regarding an established separation region on the flat plate. A change of α_1 from 0.518 to 0.61 increases the production of the turbulent specific dissipation rate ω and represents a reasonable choice for the desired separation region (see Fig. 5 stronger APG $\alpha_1 = 0.61$ in. graph). As can be observed in Fig. 7a), the velocity profiles at the inflow to the APG section are different, indicating that the change in α_1 changes the overall flow state. In addition, Fig. 7b) shows a decreased c_f distribution for $\alpha_1 = 0.61$, which leads to a separated region between $x = 1.91$ to 2.42 m (note that $c_f < 0$). By adjusting the α_1 value, a separation region similar to that in the experiments is achieved, yet located approximately $\Delta x = 0.30$ m further upstream as compared with the experiments. The total length of the separated region can be seen to be similar to that in the experiments (see Table 1). The displacement thicknesses $\delta^*_{\mathrm{sep,max}}$ at the location of the maximum separation bubble thickness $x_{\mathrm{sep,max}}$ for the experiments ($x_{\mathrm{sep,max}} = 2.55$ m) and the FP2D computations ($x_{\mathrm{sep,max}} = 2.25$ m) have a value of 71.3 and 76.2 mm, respectively. The separation bubble height for the FP2D case at this streamwise position is $h_{\mathrm{sep,max}} = 26$ mm. Lögdberg et al. [13] report a separation bubble height of $h_{\mathrm{sep,max}} = 17$ mm. The displacement thicknesses $\delta^*_{\mathrm{sep,max}}$ at $x_{\mathrm{sep,max}}$ for the experiments and the FP2D computations have a value of 71.3 and 76.2 mm, respectively. Likewise, the momentum boundary-layer thicknesses $\theta_{\mathrm{sep,max}}$ for the experiments and the FP2D computations have a value of 14.75 and 13.5 mm, respectively. Therefore, the shape factors $H_{12,\mathrm{sep,max}}$ at $x_{\mathrm{sep,max}}$ have a value of 4.90 and 5.63 for the experiments and the FP2D computations, respectively. The results can be regarded as being satisfactorily close to the experimental data.

A comparison study of certain boundary-layer parameters with flow control at the VG planes for $x_{\mathrm{VG}} = 1.10$ m and $x_{\mathrm{VG}} = 1.60$ m is given in Table 2. This was done in order to show the quality of comparability between computations and experiments with VGs. In general, the computational results show good agreement with experimental data. It must be mentioned that the boundary layer is already thickened under the influence of the APG at $x_{\mathrm{VG}} = 1.60$ m. Consequently, larger differences in δ_{99} for $x_{\mathrm{VG}} = 1.60$ m compared with $x_{\mathrm{VG}} = 1.10$ m (located in front of the APG region) occur due to the different boundary conditions of the experiments and the computations.

Table 2 Boundary-layer parameters at the position of the VG for two different VG positions, VG2D computations compared with experiments

Case	x_{VG}, m	δ_{99}, mm	$h_{\mathrm{VG}}/\delta_{99}$	δ^*, mm	h_{VG}/δ^*
Experiments case 2	1.10	15.0	1.20	3.33	5.41
VG2D	1.10	17.0	1.06	2.89	6.23
Experiments case 2	1.60	29.0	0.62	6.42	2.80
VG2D	1.60	38.0	0.47	6.39	2.82

This rather ad hoc method can be justified by the fact that the investigations focus on flow separation control using VGs and the

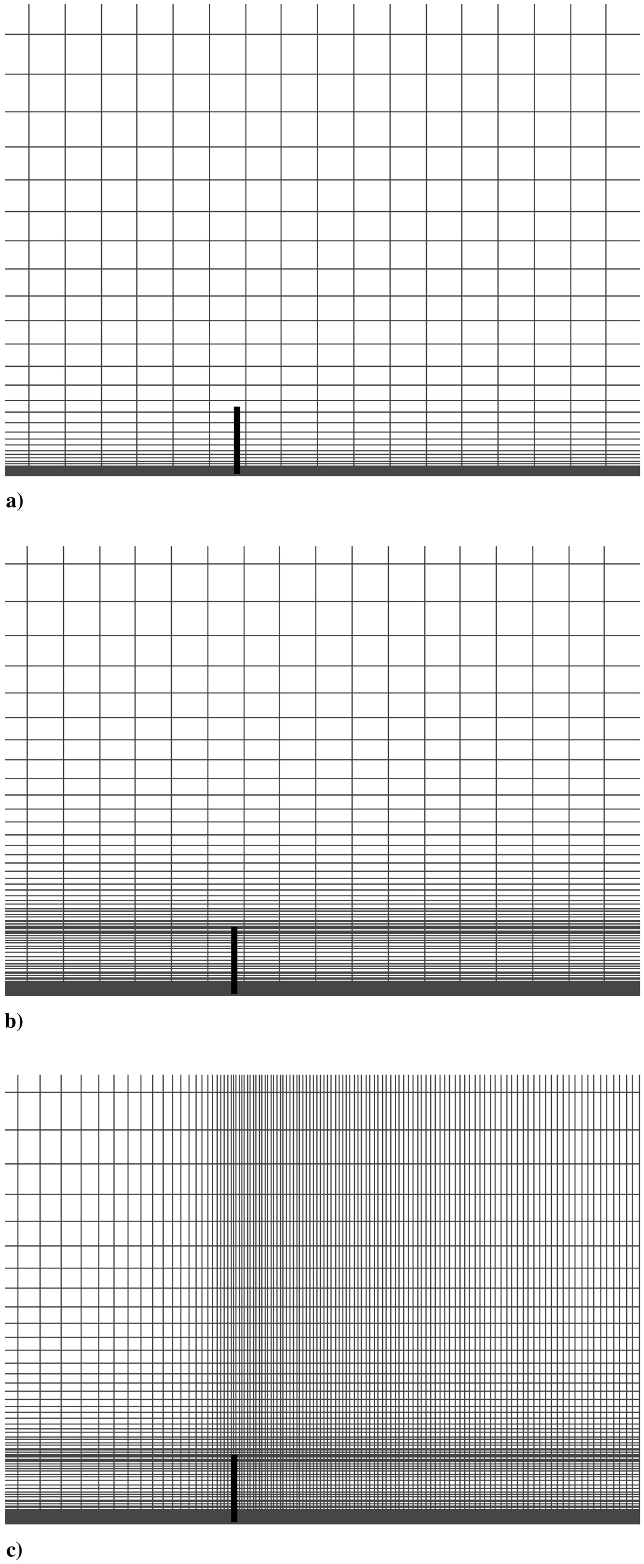

Fig. 8 Three different grids for the VG2D grid refinement study: a) baseline, b) fine-*y*, and c) fine-*xy* grid. The position and height of the modeled VG is indicated as a vertical black line.

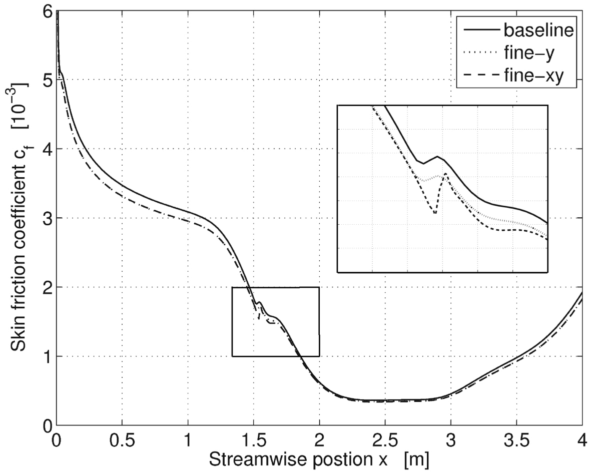

Fig. 9 Grid comparison study: local skin friction distributions for the baseline, the fine-*y*, and the fine-*xy* grids including a detail plot that shows the skin friction change around the VG model location for each grid.

resulting differences in skin friction. The computations were set up such that the baseline flow has a separation in line with the experiments. Hence, the intention was not to suggest a new turbulence model.

B. Grid Refinement Study

A grid refinement study was carried out for the VG2D computations in order to examine results regarding the necessary grid resolution. In particular, the resolution in the wall-normal direction around the VG model tip and the streamwise resolution in the vicinity and downstream of the VG model location are of interest. Three different grids were generated (see also Fig. 8). The baseline grid in Fig. 8a consists of 321 × 55 nodes in the x and y directions without any refinement region around the VG. The fine-y grid (321 × 100 nodes, Fig. 8b) is refined only in the wall-normal direction with the grid points clustered around the VG tip ($y = h$) where the $\Delta\overline{u_i'u_j'}$ forcing is strong. The fine-xy grid (536 × 100 nodes) has the same distribution in the wall-normal direction as the fine-y grid, but is further refined in the streamwise direction in the vicinity of the modeled VG (see Fig. 8c). The resulting skin friction coefficient distribution plots are given in Fig. 9. As can be observed, the refinement in the wall-normal direction gives a somewhat lower skin friction upstream of the VG position. However, it is sufficient to use the baseline grid without any local refinement regions around the VG tip, in the vicinity and downstream of the VG model location. Downstream of the VG position, the skin friction reaches a state of grid independence with an error of less than 5% compared with the refined grids which are seen to give very similar results over the whole flat plate. Therefore, the baseline grid was chosen for the examination of the APG flat plate flow with the VG model. An important result of this grid study is that the VG model may be placed anywhere the mesh resolution compares to its original location without the need for further remeshing. This is very advantageous when a parameter variation of the VG model location is carried out (see also Sec. V for more details).

V. Results

This chapter presents the results of the FP2D, the VG2D, and the VG3D computations. Experimental c_f and c_p distributions with VGs were unfortunately not available. A baseline case was set and a VG position, a VG setup, and a circulation per unit width variation as examined in Lögdberg et al. [13] are carried out. VG3D computations were nevertheless only carried out for the baseline case with $x_{\mathrm{VG}} = 1.54$ m. Both for the baseline case and for the VG parameter variations, skin friction plots are presented in the subsequent sections. Velocity profiles for the FP2D case, located in the middle of the separation bubble at $x_{\mathrm{sep,max}} = 2.25$ m, are also presented and compared with experiments for the VG2D and VG3D baseline cases. The VG position and the circulation per unit width variation computational results are moreover compared quantitatively with each other and corresponding experiments.

A. Baseline Case

The same VG setup as in the experiment is used for the VG2D and VG3D baseline cases. The trailing edge of the fully resolved VGs and the VG model forcing plane were consequently located at $x_{\mathrm{VG}} = 1.54$ m.

Figure 10a shows the wall pressure coefficient distribution of the experiments without VGs. They describe a steep increase in wall pressure downstream of $x_{\mathrm{APG,start}} = 1.25$ m. The constant increase of c_p remains until $x \approx 2.00$ m from where the c_p distribution flattens out and quickly develops another constant slope region from $x = 2.25$ m up to approximately $x_{\mathrm{APG,end}} = 2.95$ m. This region can be identified as the separated region (cf. Table 1).

The FP2D uncontrolled computation gives a very similar c_p distribution, showing a slightly steeper pressure increase and a separation region beginning at $x = 1.91$ m. The skin friction plots in Fig. 10b present additional information about the separation region. As expected, c_f decreases quickly from the leading edge and starts to decrease even faster beginning with the APG region at $x = 1.25$ m.

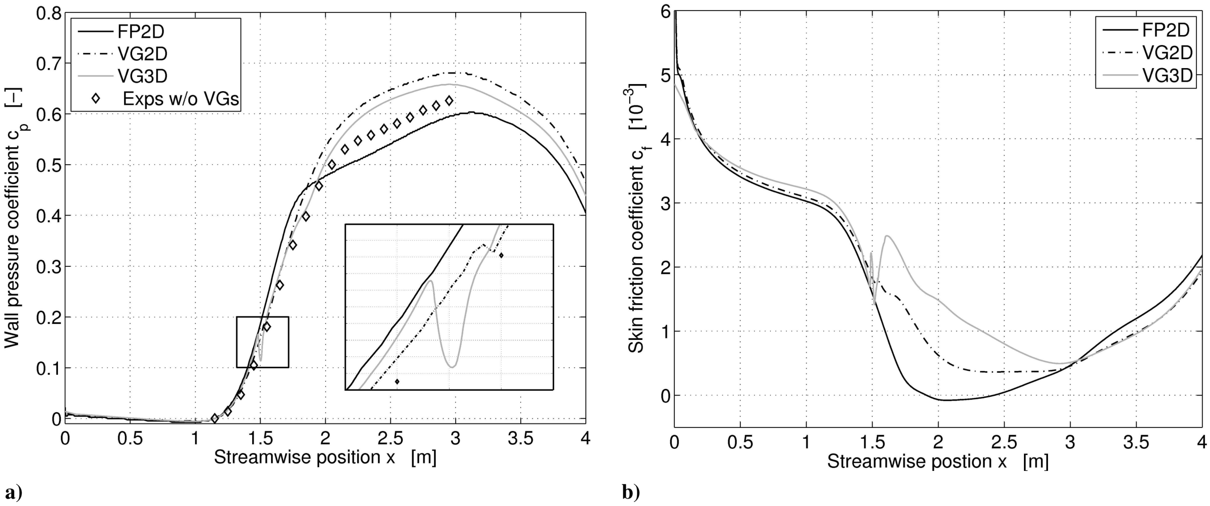

a) b)

Fig. 10 Streamwise distribution of a) the local skin friction coefficient including a detail plot showing the pressure drops for VG2D and VG3D at the VG position and b) the local wall pressure coefficient for the FP2D case, the VG2D and VG3D baseline cases with $x_{\mathrm{VG}} = 1.54$ m, and experiments without VGs [only (a)].

Table 3 The circulation per unit width, the VG height, the VG position $x_{\mathrm{VG,exp}}$ from the experiments, the resulting flow state from experiments, and the VG position x_{VG} of the VG2D computations

γ_e, m/s	h_{VG}, mm	$x_{\mathrm{VG,exp}}$, m	Flow state	x_{VG}, m
3.8	18	1.10	Attached	0.80
3.1	18	1.60	Attached	1.30
1.4	18	2.00	Attached	1.70
1.0	10	2.00	Separated	1.70

The skin friction coefficient drops below zero between $x = 1.91$ to 2.42 m, describing the exact location of the back flow region close to the wall for the FP2D computation (cf. Table 1).

The VG2D results in Fig. 10a show how the application of the VG model affects the c_p distribution along the flat plate. It can be observed that the pressure distribution is slightly weaker between $x = 1.25$ and 1.85 m when compared with FP2D computations. After that, the pressure increase is much stronger than for the uncontrolled case, indicating that the separation region has vanished. This result can be confirmed and observed in Fig. 10b where the c_f distribution does not decrease below zero anywhere.

Spanwise averaged VG3D results including the fully resolved VGs are also presented in Fig. 10. It can be observed that the c_p distribution is generally slightly lower downstream of $x_{\mathrm{VG}}=$ 1.54 m, yet very similar to the VG2D results. The pressure loss across the VGs and the VG model location is also shown in detail in Fig. 10a. Compared with the VG2D results, the c_f distribution for the VG3D case describes a higher skin friction level throughout the whole APG section except in the vicinity of the VGs (see Fig. 10b). This difference is a result of the VG3D vortex structures which are resolved in the computational domain and survive very far downstream. Compared with that, the VG2D turbulent stresses including the vortex stress contribution decay quickly downstream of the VG model plane. Downstream of the APG section ($x > 2.95$ m), the curve collapses with the VG2D curve over a short section but diverges again within the FPG section.

The extended Reynolds stresses $\overline{v_i'v_j'}$ from Eq. (7) including the Reynolds stresses $\overline{u_i'u_j'}$ and the additional vortex stresses $\Delta\overline{u_i'u_j'}$ from Eq. (4) from the VG2D are compared with the spanwise averaged resolved computations (VG3D) at four different streamwise planes ($x = 1.54$, 1.60, 1.70, and 1.80 m) and are given in Figs. 11a–11d. Note that there is no forcing of the $\Delta\overline{u'v'}$ and $\Delta\overline{u'u'}$ stresses for the VG2D at the VG model forcing plane $x = 1.54$ m. There, the stresses describe a very similar distribution compared with the incoming turbulence (FP2D). Nevertheless, the total $\overline{u'v'}$ stresses of the VG model are increasing for the subsequent streamwise locations due to production and redistribution even though they do not totally catch up with results from resolved computations. In contrast to that, the VG2D $\overline{u'u'}$ stresses do not seem to change substantially when traveling downstream. Figures 11a and 11b show that the resolved computations reveal much stronger spanwise averaged $\overline{u'v'}$ and $\overline{u'u'}$ stresses due to the existing vortex structures in the computational domain. The total $\overline{v'v'}$ and the total $\overline{w'w'}$ stress distributions (Figs. 11c and 11d) clearly show the effect of the vortex stress forcing

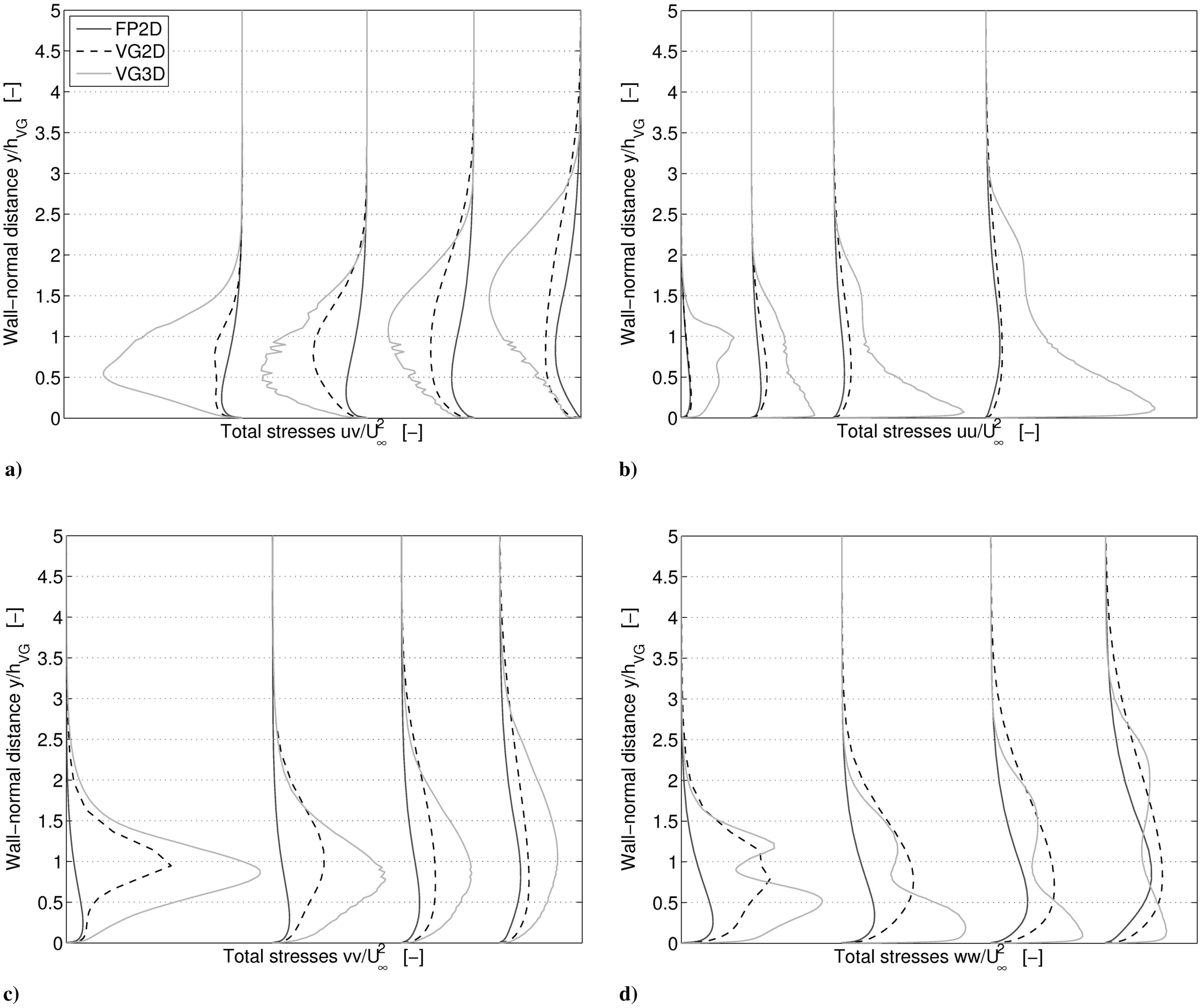

Fig. 11 VG baseline case: total stresses $\overline{u'v'}$, $\overline{u'u'}$, $\overline{v'v'}$, and $\overline{w'w'}$ including vortex and turbulence stresses from VG2D computations compared with spanwise averaged results from resolved computations (VG3D) at streamwise positions $x = 1.54, 1.60, 1.70,$ and 1.80 m. Also, the Reynolds stresses from the FP2Ds are included for comparison.

at the first streamwise position. Still, differences between the VG model results and the fully resolved results occur both in terms of amplitude and structure but the qualitative description of the stresses is reasonable. Redistribution and diffusion result in weaker stresses further downstream. The VG model could be improved in order to investigate a more complete vortex stress forcing, including the $\Delta\overline{u'u'}$ and the $\Delta\overline{u'v'}$ stress contributions. This aspect is worth a thorough investigation and a study is currently ongoing.

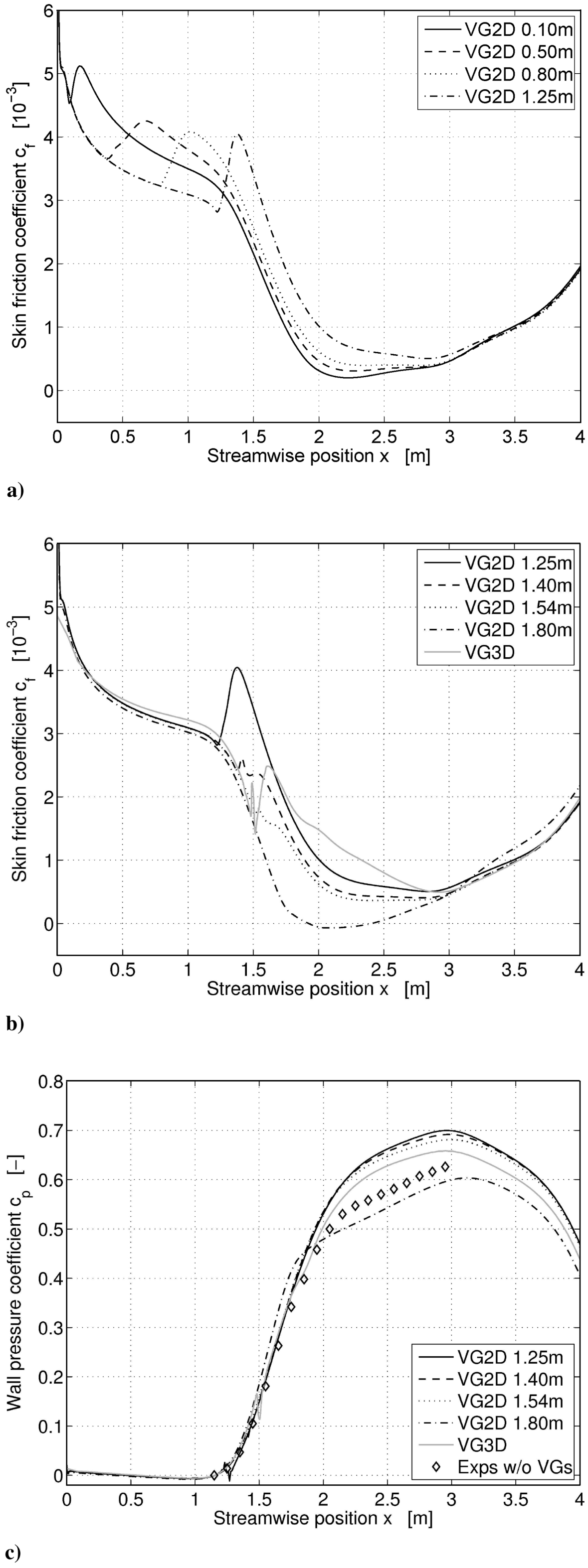

Fig. 12 Streamwise distributions of a–b) the local skin friction coefficient distributions for the VG position variation and for the VG3D baseline computations with $x_{\mathrm{VG}} = 1.54$ m and c) the local wall pressure coefficient distributions for the VG position variation, for VG3D, and for experiments without VGs.

B. Vortex Generator Position Variation

Seven streamwise VG positions using the VG model are examined here: $x_{\mathrm{VG}} = 0.10, 0.50, 0.80, 1.25, 1.40, 1.54$, and 1.80 m (see also Figs. 12a and 12b). The first three positions are located in the ZPG section and the last four positions in the APG section, whereas the most downstream located VG at $x_{\mathrm{VG}} = 1.80$ m is very close to the separation region ($x_{\mathrm{sep}} = 1.91$ m). The VG2D computations show distinct c_f peaks at the VG positions (except for $x_{\mathrm{VG}} = 1.80$ m), similar to the VG3D computations. The flow separation prevention works well even though the effectiveness in enhancing the c_f distribution is strongly dependent on the VG location. It can be seen that all VG positions, except the very downstream, prevent flow separation successfully. Within the APG region, the skin friction is generally further increased the further upstream the VG is located. By comparing the results in Figs. 12a and 12b, it can be observed that there must exist a global optimal VG position in the vicinity of $x = 1.25$ m. Further computations may be helpful to locate the exact position but this was not the aim of this investigation.

Figure 12c presents the c_p distributions for the four streamwise positions $x_{\mathrm{VG}} = 1.25, 1.40, 1.54$, and 1.80 m. Here, the tendency of a higher pressure increase in the APG region is clearly visible the more upstream the VGs are located. This is the result of higher streamwise velocities around the VGs due to a thinner boundary layer further upstream. Stronger vortices are therefore generated that in turn have a stronger effect on flow separation prevention, resulting in lower total pressure losses.

Further downstream at $x_{\mathrm{VG}} = 1.80$ m, the c_f and c_p distributions in Figs. 12b and 12c are almost equal to the FP2D case (cf. Figures 10a and 10b). The separation bubble is still present because the boundary layer is already substantially decelerated at $x_{\mathrm{VG}} = 1.80$ m so that only very weak vortices are generated. These vortices do not to have any significant effect on flow separation prevention.

The trend that an increased distance between the VGs and the separation region has advantages for flow separation control is valid in the range of positions studied here. Locating the VGs further upstream, the generated vortices may nevertheless encounter sooner breakdown or strong diffusion which in turn weakens the positive influence on the mean flow before they actually reach the separated region.

Velocity profiles for the VG position variation and the VG3D baseline case at $x_{\mathrm{sep,max}} = 2.25$ m are presented in Fig. 13. The VG3D computations provide, besides the spanwise averaged

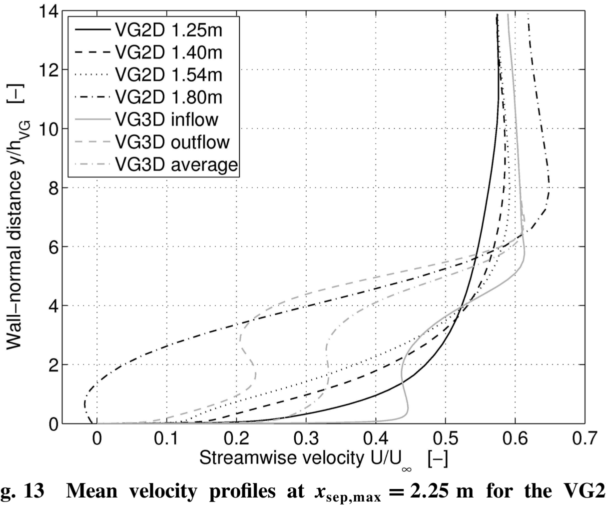

Fig. 13 Mean velocity profiles at $x_{\mathrm{sep,max}} = 2.25$ m for the VG2D streamwise position variation, and for the VG3D baseline computations with $x_{\mathrm{VG}} = 1.54$ m at inflow and outflow positions as well as the corresponding averaged velocity profile for VG3D.

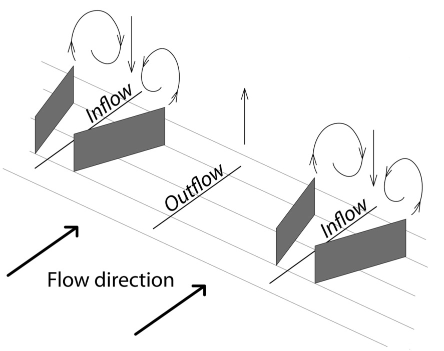

Fig. 14 The spanwise inflow and the outflow planes of the VG3D computations.

velocity profile, two additional velocity profiles at an inflow and an outflow position in the spanwise direction. These two positions correspond to the inflow and outflow positions from Lögdberg et al. [13] (see also Fig. 14). The inflow position is defined as the midposition between two VG vanes in a counter-rotational setup. Likewise, the outflow position is defined as the midposition between two VG pairs.

It can be observed from Fig. 13 that the four VG2D model computations indicate conforming trends for all streamwise positions. The further downstream the VG is applied, the lower are the streamwise velocities close to the wall, indicating less momentum mixing in the boundary layer. The computations for $x_{\mathrm{VG}} = 1.80$ m result in reversed flow, being consistent with the c_f distribution in Fig. 12b. The three plots of the VG3D computations present the results of the inflow, outflow, and the spanwise averaged velocity profiles. In general, they illustrate the velocity defect from the fully resolved VG vanes. First, high-momentum containing fluid is pushed down towards the wall at the inflow position, increasing the near-wall velocity (gray solid line). Here, it can be observed how the flow is accelerated close to the wall. Secondly, low-momentum fluid is pushed upwards at the outflow position, leading to lower velocities near the wall (gray dashed line). The corresponding velocity profile for $x_{\mathrm{VG}} = 1.54$ m fits in between the VG3D velocity profiles at the inflow and outflow positions, yet lacking the velocity defect. However, the VG2D profile is not matching the spanwise averaged VG3D profile (gray dashed–dotted line), giving a lower near-wall velocity distribution and lacking the averaged velocity defect further away from the wall. Nevertheless, it can be stated that the VG2D velocity profiles are consistent with each other regarding the trend of the VG position variation. The plots also confirm the c_f and the c_p distributions in Figs. 12b and 12c. Moreover, the results of the VG3D computations show how the vortex structures propagate away from the wall boundary and therefore support the important role of boundary-layer mixing effects for flow control.

C. Circulation per Unit Width Variation

Lögdberg [12] carried out a parameter variation study regarding the VG array streamwise location including different VG heights. This experimental study is used for a qualtitative comparison with the VG2D computations. The experimental data were parameterized by means of the circulation per unit width for a VG array which is defined as

$$\gamma_e \equiv 2k \frac{h_{\mathrm{VG}} U_{\mathrm{VG}}}{D} \tag{10}$$

where k is a coefficient that takes the VG geometry into account (see Angele and Muhammad-Klingmann [23]) h_{VG} the VG height, U_{VG} the VG tip velocity, and D the distance between VG pairs in the spanwise direction. For the computations, $D = 150$ mm. In accordance with Lögdberg et al. [13], a value of $k = 0.6$ is used, resulting in a circulation per unit width for the present parameter variation study $\gamma_e = 66.67 h_{\mathrm{VG}} U_{\mathrm{VG}}$ m^{-1}. Thus, γ_e is dependent only on the VG height h_{VG} and the VG tip velocity U_{VG} which is equivalent to the streamwise position x.

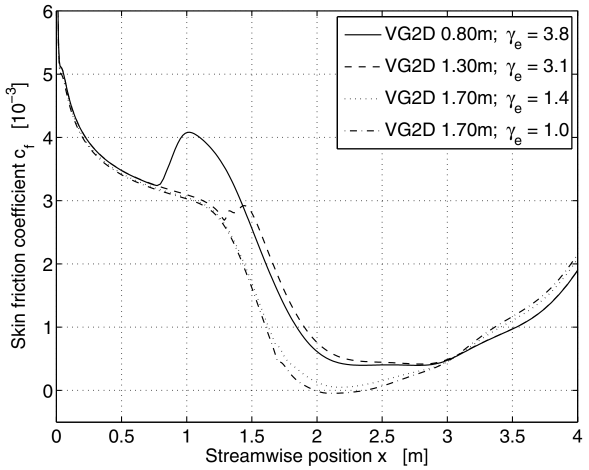

Fig. 15 Local skin friction coefficient distributions for the VG2D circulation per unit width variation, in accordance with Table 3.

To compare experiments and computations with each other, the same parameterization is also adopted in the computations, and values for γ_e were matched. This means that the VG height and the VG streamwise position need to be adjusted in order to give comparable γ_e values. The first matter is straightforward to implement into computations (identical VG heights), whereas the latter means an adjustment of the streamwise VG position in such a way that VG tip velocities correspond to VG tip velocities in experiments. Since the separation bubble location and length as well as the evolution of the boundary layer from computations do not exactly match experiments, a coordinate transformation and therefore an upstream shifting of the VG position is necessary. As a result, the VG must be shifted $\Delta x = 0.30$ m upstream in order to match experimental γ_e values. Table 3 presents the setup for both, the experiments and the VG2D computations, as well as the resulting flow state from experiments.

Skin friction coefficient results of this study are presented in Fig. 15, though only for the VG2D computations since skin friction data from experiments are not available. Yet, the primary focus of this VG2D study was to examine and compare the flow state prediction capabilities. From Fig. 15, it can be observed that the overall trend of the flow state from Table 3 is predicted correctly by the VG model. Computations for the first three cases regarding the c_f plots show separation prevention ($c_f > 0$ everywhere). In contrast to that, a reduction in h_{VG} from 18 to 10 mm results in separated flow as the in experiments (see the last case for $\gamma_e = 1.0$ m/s in Table 3). Again, the application of the VG model further upstream at $x_{\mathrm{VG}} = 0.80$ m and $\gamma_e = 3.8$ m/s shows less effectiveness for flow separation prevention than for $x_{\mathrm{VG}} = 1.30$ m, confirming the overall trend of Fig. 12.

D. Vortex Generator Setup Variation

Another interesting aspect to examine is the difference in flow separation effectiveness between co- and counter-rotational VG setups (see Fig. 16). Here, four different setups were investigated: two counter-rotational settings, one given by a common-flow-down and another one by a common-flow-up setting (Figs. 16a and 16b, respectively). Furthermore, two corotating settings were examined: one with a VG vane distance $D/2 = 75$ mm, and another setting with an increased VG vane distance of $D = 150$ mm, that doubles the distance between VG vanes and therefore decreases the total VG vane density in the VG array by a factor of 2 (see Figs. 16c and 16d, respectively).

In Fig. 17, the results of this comparison show that counter-rotational systems are more efficient than corotating systems. This is in accordance with previous experimental results [3]. The c_f distributions for the corotating setups do not show much improvement when the VG vane density is doubled (when VG

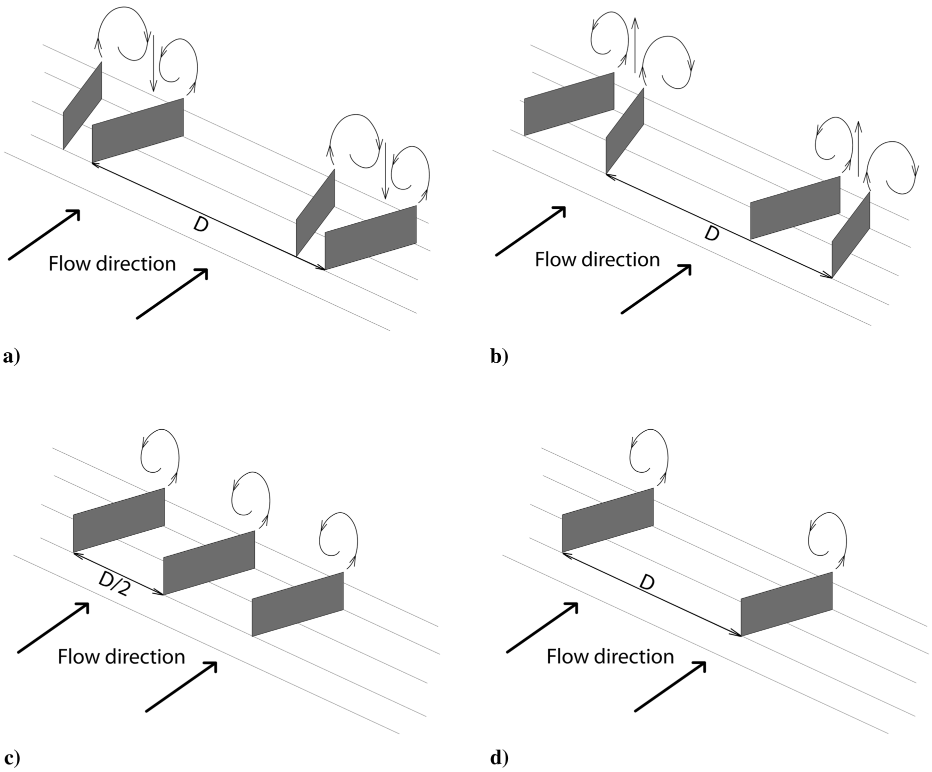

a) b) c) d)

Fig. 16 Different VG setups: a) counter-rotational common-flow-down, b) counter-rotational common-flow-up, c) corotating with a spanwise VG vane distance $D/2$, and d) corotating with a spanwise VG vane distance D.

vane distance decreases from D to $D/2$; see Fig. 17). This is a consequence of the superposition of the single vortex velocity fields from Eq. (3), resulting from the modeled VG array. Here, the induced vortex velocities partly weaken and damp out each other and this effect is higher the closer the VG vanes are located to each other, in accordance with Lin [4].

However, the VG model does not distinguish between common-flow-up and common-flow-down settings as can be observed in Fig. 17. Here, the c_f distributions lie on top of each other. The reason for that is the spanwise averaging of the second-order statistics at the VG model forcing plane which results in identical contributions for the $\Delta\overline{u'w'}$ forcing. Therefore, the additional vortex stresses are also identical for both counter-rotational setups and the current VG model approach from Eq. (4) can hence not distinguish between these cases. However, experiments [2] show higher efficiency for common-flow-down setups since the vortices remain longer and closer to the wall, having a better and more persistent effect on flow separation prevention.

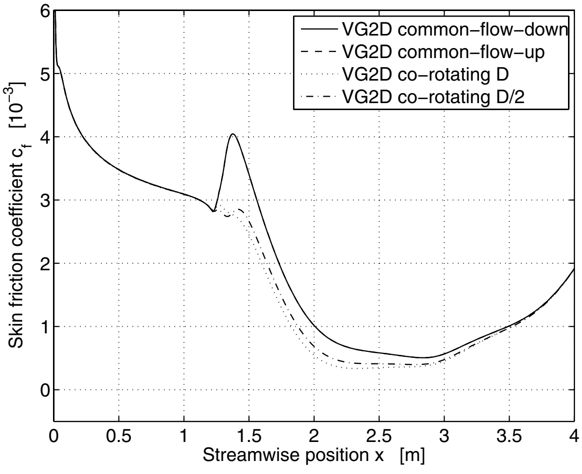

Fig. 17 Local skin friction coefficient distributions for different VG setups in accordance with Fig. 16 with a VG model forcing plane $x_{\mathrm{VG}} = 1.25$ m.

VI. Conclusions

This investigation has shown the capabilities of the statistical VG model to mimic the effects of VG arrays in APG boundary-layer flow by means of introducing additional vortex stresses to the turbulence Reynolds stresses. Wall pressure and skin friction coefficient distribution plots of the VG2D computations in APG boundary layer have shown that flow separation prevention can be attained for several different configurations. Qualitative parameter variation studies and a comparison between experimental results, VG2D computations, and VG3D computations were carried out. The trends obtained in these studies successfully showed the capability of the VG model to predict flow separation prevention for identical VG setups such as in experiments and fully resolved computations. Nevertheless, quantitative differences between the VG model and the fully resolved VG results exist. In particular, the shear stress component $\Delta\overline{u'v'}$ is not directly forced but rather developed as a result of the production and redistribution of energy. The results indicate that the development of the shear stress component is slower and weaker than that shown in experiments. More effort should be made in formulating an improved VG model, enabling even the shear stress forcing.

A result of this examination is that the VGs' streamwise position as well as the height and the setup of the VG model strongly influence the skin friction distribution and therefore, the effectiveness of the modeled flow control devices. The overall trends and tendencies from the parameter variations using the VG model show that there exists an optimal streamwise position for the VGs applied in the present APG boundary-layer flow case. It can be concluded that the VGs should be placed some distance upstream of the separation bubble in order to be able to generate the required vortex stresses that further develop downstream. Locating the VGs further upstream from the optimum position will generate stronger vortex stresses that in turn undergo longer-lasting diffusive processes until they reach the separation region which weakens the VGs' effectiveness. On the other hand, further downstream VG positions (also compared with the optimum) generate weaker vortex stresses with less effect on the separated flow regime due to a lower streamwise boundary-layer velocity. If the VGs are placed too close to the separation region, flow control is not attained. In total, it can be observed that all the investigated VG positions, except those very close to the separation region, give flow separation prevention.

Different combinations of the VG position and height could successfully be simulated by correctly predicting the parameter regimes for attached and separated flow when compared with the experiments. Inspection of the VG model's sensitivity to co- and counter-rotational setups showed consistency with earlier experimental results [3].

In summary, this approach of modeling passive VG vanes for flow control has proved to be promising for an application to APG boundary-layer flows. The major advantage of the VG model approach is that it is only as computationally expensive as solving the RANS equations without VGs, leading to much faster results than with conventional methods such as fully or even partly resolved VGs. Therefore, it could be used as a powerful tool for concept studies such as the optimal position of passive flow control devices. Results showed correct trends and tendencies in agreement with experiments and fully resolved computations. Nevertheless, the user must also be aware of the VG model's shortcomings.

Acknowledgments

The experiments were part of a cooperative research program between the Royal Institute of Technology Stockholm and Scania AB (publ), Sweden. Ola Lögdberg is gratefully acknowledged for providing experimental data.

References

[1] Pearcey, H. H., *Boundary Layer and Flow Control, its Principles and Applications. Part 4: Shock-Induced Separation and its Prevention by Design and Boundary Layer Control*, edited by G. V. Lachmann, Pergamon, Oxford, 1961.

[2] Pauley, W. R., and Eaton, J. K., "Experimental Study of the Development of Longitudinal Vortex Pairs Embedded in a Turbulent Boundary Layer," *AIAA Journal*, Vol. 26, No. 7, 1988, pp. 816–823. doi:10.2514/3.9974

[3] Godard, G., and Stanislas, M., "Control of a Decelerating Boundary Layer, Part 1: Optimization of Passive Vortex Generators," *Aerospace Science and Technology*, Vol. 10, No. 3, 2006, pp. 181–191. doi:10.1016/j.ast.2005.11.007

[4] Lin, J. C., "Review of Research on Low-Profile Vortex Generators to Control Boundary-Layer Separation," *Progress in Aerospace Sciences*, Vol. 38, Nos. 4–5, 2002, pp. 389–420. doi:10.1016/S0376-0421(02)00010-6

[5] Bender, E. E., Anderson, B. H., and Yagle, P. J., "Vortex Generator Modelling for Navier–Stokes Codes," American Society of Mechanical Engineers Paper 99-6919, 1999.

[6] Glauert, H., *The Elements of Aerofoil and Airscrew Theory*, 1st ed., Cambridge Univ. Press, London, 1926.

[7] Anderson, J. D., *Fundamentals of Aerodynamics*, 2nd ed., McGraw–Hill, New York, 1991.

[8] Jirásek, A., "A Vortex Generator Model and its Application to Flow Control," *Journal of Aircraft*, Vol. 42, No. 6, 2005, pp. 1486–1491. doi:10.2514/1.12220

[9] Törnblom, O., and Johansson, A. V., "A Reynolds Stress Closure Description of Separation Control with Vortex Generators in a Plane Asymmetric Diffuser," *Physics of Fluids*, Vol. 19, No. 11, 2007, p. 115108. doi:10.1063/1.2800877

[10] von Stillfried, F., Wallin, S., and Johansson, A. V., "Statistical Modeling of the Influence of Turbulent Flow Separation Control Devices," 47th AIAA Aerospace Sciences Meeting, AIAA Paper 2009-1501, Orlando, FL, 2009.

[11] Lögdberg, O., Fransson, J. H. M., and Alfredsson, P. H., "Streamwise Evolution of Longitudinal Vortices in a Turbulent Boundary Layer," *Journal of Fluid Mechanics*, Vol. 623, 2009, pp. 27–58. doi:10.1017/S0022112008004825

[12] Lögdberg, O., "Turbulent Boundary Layer Separation and Control," Ph.D. Thesis, Dept. of Mechanics, Royal Institute of Technology, Stockholm, 2008.

[13] Lögdberg, O., Angele, K., and Alfredsson, P. H., "On the Robustness of Separation Control by Streamwise Vortices," *European Journal of Mechanics B, Fluids*, Vol. 29, No. 1, 2010, pp. 9–17. doi:10.1016/j.euromechflu.2009.09.001

[14] Velte, C. M., Hansen, M. O. L., and Okulov, V. L., "Helical Structure of Longitudinal Vortices Embedded in Turbulent Wall-Bounded Flow," *Journal of Fluid Mechanics*, Vol. 619, 2009, pp. 167–177. doi:10.1017/S0022112008004588

[15] Batchelor, G. K., "Axial Flow in Trailing Line Vortices," *Journal of Fluid Mechanics*, Vol. 20, No. 4, 1964, pp. 645–658. doi:10.1017/S0022112064001446

[16] Lindgren, B., and Johansson, A. V., "Evaluation of a New Wind Tunnel with Expanding Corners," *Experiments in Fluids*, Vol. 36, No. 1, 2004, pp. 197–203. doi:10.1007/s00348-003-0705-y

[17] Angele, K. P., "Experimental Studies of Turbulent Boundary Layer Separation and Control," Ph.D. Thesis, Dept. of Mechanics, Royal Institute of Technology, Stockholm, 2003.

[18] Dengel, P., and Fernholz, H. H., "An Experimental Investigation of an Incompressible Turbulent Boundary Layer in the Vicinity of Separation," *Journal of Fluid Mechanics*, Vol. 212, No. 1, 1990, pp. 615–636. doi:10.1017/S0022112090002117

[19] Wallin, S., and Johansson, A. V., "An Explicit Algebraic Reynolds Stress Model for Incompressible and Compressible Turbulent Flows," *Journal of Fluid Mechanics*, Vol. 403, 2000, pp. 89–132. doi:10.1017/S0022112099007004

[20] Wallin, S., and Johansson, A. V., "Modelling Streamline Curvature Effects in Explicit Algebraic Reynolds Stress Turbulence Models," *International Journal of Heat and Fluid Flow*, Vol. 23, No. 5, 2002, pp. 721–730. doi:10.1016/S0142-727X(02)00168-6

[21] Hellsten, A., "New Advanced k-ω Turbulence Model for High-Lift Aerodynamics," *AIAA Journal*, Vol. 43, No. 9, 2005, pp. 1857–1869. doi:10.2514/1.13754

[22] Eliasson, P., "EDGE, a Navier–Stokes Solver for Unstructured Grids," *Proceedings to Finite Volumes for Complex Applications 3*, edited by D. Kroner and R. Herbin, Hemre Penton Science, London, 2002, pp. 527–534.

[23] Angele, K. P., and Muhammad-Klingmann, B., "The Effect of Streamwise Vortices on the Turbulence Structure of a Separating Boundary Layer," *European Journal of Mechanics B, Fluids*, Vol. 24, No. 5, 2005, pp. 539–554. doi:10.1016/j.euromechflu.2005.01.005

S. Fu
Associate Editor